Dynamics of a bistable Miura-origami structure

Hongbin Fang, Suyi Li, Huimin Ji, and K. W. Wang

Phys. Rev. E **95**, 052211 — Published 17 May 2017

DOI: 10.1103/PhysRevE.95.052211

Paper submitted to *Physical Review E*

The Dynamics of a Bistable Miura-Origami Structure

Hongbin Fang[1], Suyi Li[2*], Huimin Ji[1], and K.W. Wang[1]

[1)] Department of Mechanical Engineering, University of Michigan, Ann Arbor, MI 48109, USA
[2)] Department of Mechanical Engineering, Clemson University, Clemson, SC 29634, USA

[*]**Author for correspondence:** suyil@clemson.edu (S. Li)

Abstract:

Origami-inspired structures and materials have shown extraordinary properties and performances originated from the intricate geometries of folding. However, current state of the art studies have mostly focused on static and quasi-static characteristics. This research performs a comprehensive experimental and analytical study on the dynamics of origami folding through investigating a stacked Miura-Ori (SMO) structure with intrinsic bistability. We fabricate and experimentally investigated a bistable SMO prototype with rigid facets and flexible crease lines. Under harmonic base excitation, the SMO exhibits both intrawell and interwell oscillations. Spectrum analyses reveal that the dominant nonlinearities of SMO are quadratic and cubic, which generate rich dynamics including subharmonic and chaotic oscillations. The identified nonlinearities indicate that a third-order polynomial can be employed to approximate the measured force-displacement relationship. Such an approximation is validated via numerical study by qualitatively reproducing the phenomena observed in the experiments. The dynamic characteristics of the bistable SMO resemble those of a Helmholtz-Duffing oscillator (HDO); this suggests the possibility of applying the established tools and insights of HDO to predict origami dynamics. We also show that the bistability of SMO can be programmed within a large design space via tailoring the crease stiffness and initial stress-free configurations. The results of this research offer a wealth of fundamental insights into the dynamics of origami folding, and provide a solid foundation for developing foldable and deployable structures and materials with embedded dynamic functionalities.

I. INTRODUCTION

Origami, an ancient art of paper folding, now refers to all folding practices regardless of the materials being used. Over the last several decades, there has been a significant rise of interest in origami research across the disciplines of natural science, mathematics, architecture, and engineering. For example, plant biologists used origami folding to explain the deploying mechanisms of tree leaves, flowers, and seed capsules [1–3], and mathematicians developed algorithmic and computational tools to design complex crease patterns and analyze their folding and unfolding behaviors [4–9]. Architects and engineers have mainly explored a special kind of origami design called rigid-foldable origami, a structure consisting of rigid panels connected by ideal hinges. Many origami-inspired applications have exploited the kinematics of folding. The complex yet programmable shape transformations originated from folding have served as guidelines for many design innovations, such as architectural polyhedral surfaces [10], sandwich cores [11], aerospace deployable structures [12,13], surgical devices [14], and self-folding robots [15]. Recently, research on origami mechanics have demonstrated that folding can also be a powerful tool to tailor the structural stiffness [16–21] and generate attractive and even unorthodox mechanical properties. For example, origami-based metamaterials and structures can exhibit auxetic effects [22–24], programmable stiffness [25], high stiffness yet high reconfigurability [26], bistability and multistability [23,27–29], programmable locking and stiffness jump [24,30], and recoverable collapse [31].

Despite the significant research progress, most of the previous studies on origami have mainly focused on kinematics or static/quasi-static characteristics. Origami folding, on the other hand, could be a dynamic process and origami structures could possess rich dynamic characteristics under excitations. For example, folding and unfolding of origami can be rapid and reciprocal, and origami-based mechanical metamaterials can be a medium for elastic wave propagation and vibration transmission. Hence, origami dynamics could be important in many engineering systems and applications. Yasuda et al [32,33] investigated the nonlinear elastic wave propagation in a multiple degree-of-freedom (DOF) origami metamaterials consisting of Tachi-Miura polyhedron (TMP) cells. They demonstrated that, via utilizing the geometry-induced nonlinearity and the structure periodicity, such TMP-based tubular metamaterials can be developed into vibration and impact mitigating structures with tunable characteristics. In another study, Ishida et al. [34] developed an origami-based cylindrical

structure featuring quasi-zero stiffness and experimentally demonstrated that it can effectively isolate base excitations at low frequencies. These examples show that understanding the origami's dynamic characteristics is an essential research topic towards many potential applications. However, other than [32–34], there are no literature on origami dynamics. Furthermore, a rigorous and comprehensive framework to investigate the dynamics of origami is lacking. Instead of fully capturing the effects of folding crease lines and rotating facets, the previous origami dynamic studies simplified the structures into equivalent linkage systems with multi-bars or spring-shafts [32–34]. Such approaches are effective in reducing the problem complexity but will discard important folding-related characteristics that are unique to origami. Therefore, it is still unknown how the many newly discovered mechanical properties from origami folding, such as bistability and multistability [23,27–29], could generate interesting and useful system dynamic behaviors.

Based on the above observations, the goal of this research is to advance the state of the art through exploring origami dynamics. We focus our efforts on a stacked origami structure made up of two Miura-Ori cells [Fig. 1(a)]. Miura-Ori is the simplest degree-4 vertex pattern that possesses flat-foldability and single collinearity. Stacking two different Miura-Ori cells under geometry constraints [22,24] could yield a stacked flat-foldable structure [Fig. 1(b)]. When assigned with appropriate bending stiffness at the creases, the structure is able to exhibit bistability [27], that is, it can stay in two different folding configurations without any external aid. Note that bistability is a strong nonlinear characteristic with rich dynamics, some of which could be exploited for performance enhancement in various applications [35] such as energy harvesting [36–39], motion amplification [40,41], damping [42], sensing [43,44] and vibration cancelation [45] and isolation [46]. Despite its potential, the exploration of bistable dynamics in origami structures has never been pursued.

This research conducts a comprehensive experimental and analytical study on the dynamics of a bistable stacked Miura-ori structure (SMO) without simplifying it into an equivalent linkage mechanism. We design and fabricate a rigid-foldable origami prototype and carry out systematic dynamic tests under harmonic base excitations. Notably, we observe that the SMO structure is able to exhibit two types of dynamic responses: small-amplitude intrawell oscillations and large-amplitude interwell oscillations. Transmissibility analysis shows that the intrawell oscillation, at some frequency intervals, is able to attenuate the excitations; while the interwell oscillation will amplify the excitations. We then perform spectrum analysis on the measured

responses, which reveals that both quadratic and cubic factors are dominant in the SMO nonlinear stiffness. It is these two types of nonlinearities that induce the observed rich dynamics, including regular periodic oscillations, subharmonic oscillations, and chaotic oscillations. To validate the experimental findings, we use a third-order polynomial to approximate the measured force-displacement curve of the SMO structure and apply it in numerical investigations. Simulation results capture the experimental observations, illustrating the validity of the nonlinearity identification. Some heuristic discussions on the SMO structure and its dynamics are presented, which offers directions for future research. We first note that the SMO structure exhibits an asymmetric bistable potential profile that can be described by a Helmholtz-Duffing oscillator (HDO). Such an observation indicates that the established tools (e.g., the harmonic balance method) and insights of HDO can be utilized to predict the bistable origami dynamics. We also demonstrate that the SMO structure's bistability can be effectively programmed in terms of the stable well positions, the well depth, and the asymmetry level between the wells, without changing the origami crease pattern.

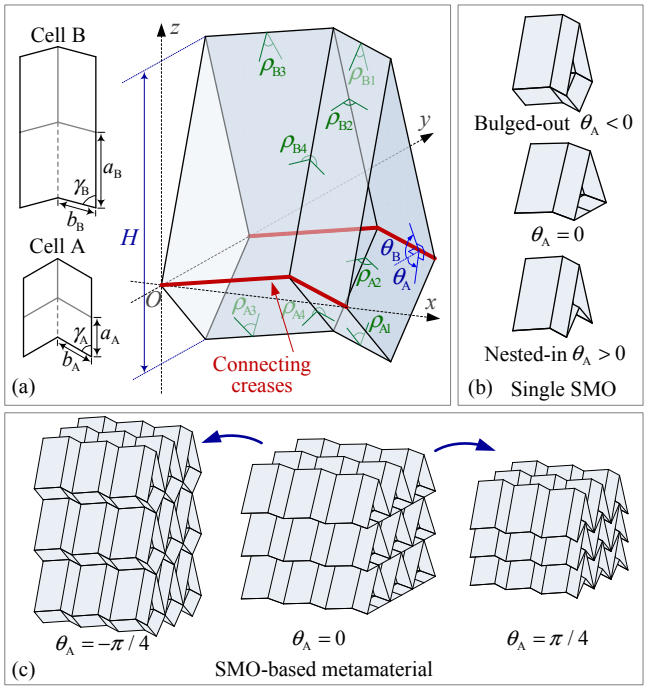

FIG. 1. Geometry and kinematics of the SMO structure. (a) Geometry of a single SMO structure. The plane crease pattern of the bottom cell A and top cell B are given, with the internal solid and dashed lines indicating the "mountain" and "valley" creases, respectively. (b) A single SMO structure at the bulged-out ($\theta_A < 0$), intermediate ($\theta_A = 0$), and nested-in ($\theta_A > 0$) configurations. (c) Origami-based metamaterials expanded from SMO units, shown in three states.

This paper is organized as follows. Sec. II introduces the geometric design, folding kinematics, and bistability of the SMO structure. Sec. III presents the analysis of the dynamic experimental results based on an SMO prototype. The key nonlinear factors of the SMO structure are identified and are qualitatively verified through numerical investigation, as illustrated in Sec. IV, and heuristic discussions are presented in Sec. V. Finally, Sec. VI concludes with a summary and remarks on potential applications.

II. ORIGAMI MODELING AND PROTOTYPE

A. Origami geometry and kinematics

We begin by characterizing the Miura-Ori geometry and folding kinematics. Miura-Ori is a particular kind of degree-4 vertex with a pair of collinear creases and reflectional symmetry about this crease. A Miura-Ori cell crease pattern can be defined by the lengths of two adjacent crease lines (a_k , b_k) and an angle γ_k between them [Fig. 1(a)], where the subscript "k (=A, B)" indicate the two connected cells A and B. Considering the rigid-folding scenario, Miura-Ori retains a single degree-of-freedom (DOF) for folding. Its folding motion can be described by the folding angle θ_k $(k = A, B)$ defined as the dihedral angle between the facet and the reference $x-y$ plane [Fig. 1(a)]. Without loss of generality, we designate the smaller cell with the shorter crease length as the bottom cell A [Fig. 1(a)]. To ensure kinematic compatibility between the two cells so that they keep connected during folding, the following relations have to be satisfied [22]:

$$b_{\mathrm{A}} = b_{\mathrm{B}} = b, \quad \frac{\cos\gamma_{\mathrm{B}}}{\cos\gamma_{\mathrm{A}}} = \frac{a_{\mathrm{A}}}{a_{\mathrm{B}}}. \tag{1}$$

With these kinematic constraints, the folding angles θ_{A} and θ_{B} follow the following relationship [22]:

$$\theta_B = \arccos\left(\cos\theta_A \frac{\tan\gamma_A}{\tan\gamma_B}\right). \tag{2}$$

Note that θ_{A} ranges between $-\pi/2$ and $\pi/2$ while θ_{B} keeps positive such that cell A bulges out of the larger cell B when $\theta_{\mathrm{A}} < 0$ and nests into B otherwise. In what follows, for clarity, we denote the configuration with $\theta_{\mathrm{A}} < 0$ as 'bulged-out' and otherwise as 'nested-in' [Fig. 1(b)].

Particularly, Eq. (2) indicates a non-unique angle relation between the folding angles of the

two cells. For one θ_B angle, θ_A could take two values with the same magnitudes but opposite signs corresponding to the bulged-out and nested-in configurations, respectively. The only exception occurs at the minimum value of θ_B, which corresponds to a flat state of cell A (i.e., $\theta_A = 0$). We will show in later discussion that such non-unique relationship is the origin of the elastic bistability.

Miura-Ori's folding motion can also be depicted by the dihedral angles between each two adjacent facets ρ_{ki} $(k = A, B;\ i = 1,2,3,4)$ [Fig. 1(a)], we have:

$$\begin{aligned} &\rho_{k1} = \rho_{k3} = \pi - 2\theta_k, \\ &\sin\frac{\rho_{k2}}{2} = \frac{\cos\theta_k}{\sqrt{1-\sin^2\theta_k \sin^2\gamma_k}}, \\ &\rho_{k4} = 2\pi - \rho_{k2}. \end{aligned} \tag{3}$$

For the bulged-out configuration ($\theta_{\mathrm{A}} < 0$), we assign $\rho_{\mathrm{A}2} \in (\pi, 2\pi)$; for the nested-in configuration ($\theta_A > 0$), $\rho_{\mathrm{A}2} \in (0, \pi)$. The dihedral angles at the connecting creases are given as $\rho_{\mathrm{C}} = \theta_{\mathrm{B}} - \theta_{\mathrm{A}}$.

We remark here that the 3-dimensional (3D) SMO structure possesses high potential to be expanded into a 3D origami-based metamaterial [Fig. 1(c)] [22,47]. If all the SMO units are ideally connected under the rigid-foldable assumption, the overall periodic SMO metamaterial is still rigid-foldable with a single DOF for folding.

B. Elastic bistability

When subjected to an external force, the Miura-origami structure can deform by both crease folding and facet bending, depending on the relative stiffness difference between the facets and the creases [20]. Here in order to investigate the bistable dynamics without unnecessary complexities, we assume the facets to be rigid, and the creases to be elastic hinges of prescribed torsional stiffness. We assign k_{A} and k_{B} as the torsional spring stiffness per unit length for the creases in cell A and cell B, respectively; and k_{C} as the torsional stiffness at the connecting creases between the two cells. Then the torsional stiffness constants (K_{ki} and K_{C}) corresponding to each dihedral angle (ρ_{ki} and ρ_{C}) can be determined. In cell A, $K_{\mathrm{A1}} = K_{\mathrm{A3}} = k_{\mathrm{A}} b$, $K_{\mathrm{A2}} = K_{\mathrm{A4}} = k_{\mathrm{A}} a_{\mathrm{A}}$; in cell B, $K_{\mathrm{B1}} = K_{\mathrm{B3}} = k_{\mathrm{B}} b$, $K_{\mathrm{B2}} = K_{\mathrm{B4}} = k_{\mathrm{B}} a_{\mathrm{B}}$; and at the connecting creases, $K_{\mathrm{C}} = k_{\mathrm{C}} b$. Hence the total potential energy of an SMO structure originating from the torsional springs yields

$$\Pi = \frac{1}{2}\left[\sum_{i=1}^{4} K_{\mathrm{A}i}\left(\rho_{\mathrm{A}i}-\rho_{\mathrm{A}i}^{0}\right)^{2}+\sum_{i=1}^{4} K_{\mathrm{B}i}\left(\rho_{\mathrm{B}i}-\rho_{\mathrm{B}i}^{0}\right)^{2}+4K_{\mathrm{C}}\left(\rho_{\mathrm{C}}-\rho_{\mathrm{C}}^{0}\right)^{2}\right], \tag{4}$$

where ρ_{Ai}^{0}, ρ_{Bi}^{0} and ρ_{C}^{0} are the dihedral angles corresponding to the stress-free stable folding configuration ($\theta_{\mathrm{A}}=\theta_{\mathrm{A}}^{0}$) where no crease is deformed from its "natural" stress-free shape.

Upon adjusting the torsional stiffness and the stress-free configuration, the system potential can be programmed. Fig. 2(a) and 2(b) display the effects of torsional stiffness coefficients and the stress-free configuration on the structure potential, respectively. The SMO structure design parameters are listed in Table 1; in what follows, unless noted otherwise, all studies are based on this design. Fig. 2 reveals that the structure's potential energy with respect to the folding angle is highly nonlinear, even though the constituent torsional stiffness of the creases are linear. Such nonlinearity is due to the intrinsic nonlinear geometric relationship between the dihedral angles (ρ_{ki} and ρ_{C}) and the folding angle (θ_{A}) shown in Eq. (3). Particularly, if the torsional stiffness of cell B (i.e., $k_{\mathrm{B}}=\mu k$, where μ is a positive constant) is significantly higher than k_{A} and k_{C}, or the stress-free folding angle (θ_{A}^{0}) deviates further from 0, the potential curve begin to show a twin-well scenario, which is a characteristic feature of bistability. The origin of this elastic bistability is directly related to the $\theta_{\mathrm{A}}-\theta_{\mathrm{B}}$ relation given in Eq. (2). Note that the two stable configurations will have qualitatively different shapes: if the stress-free configuration is designated to have a nested-in shape, the other stable configuration will be bulged-out; and vice versa. An interesting feature that distinguishes the SMO structure with other bistable structure is its intrinsic asymmetric bistability. Fig. 2 reveals that the two stable configurations are not symmetric in either positions or potential values.

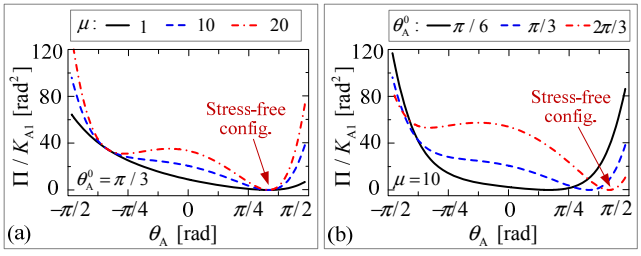

FIG. 2. The normalized potential energy landscape with respect to the folding angle θ_{A}. (a) With stress-free configuration $\theta_{\mathrm{A}}^{0}=\pi/3$, bistability (dot-dashed) shows up when $k_{\mathrm{B}}=\mu k$ is significantly higher than $k_{\mathrm{A}}=k$. (b) With $k_{\mathrm{B}}=10k$, bistability (dot-dashed) shows up when the stress-free configuration θ_{A}^{0} is far away from 0. Note that the bistability profile presents obvious asymmetry.

TABLE 1. SMO structure design

Parameters	Values	Parameters	Values
$b_A = b_B = b$	38.1 mm	γ_A	60°
a_A	38.1 mm	γ_B	75°
$k_A = k_C$	k	k_B	μk

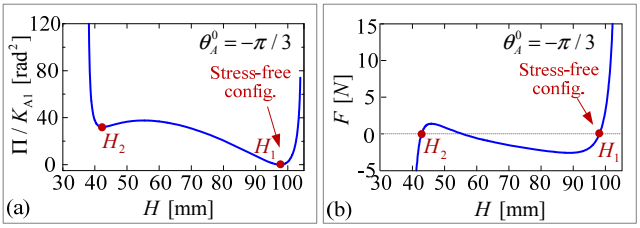

FIG. 3. Asymmetric bistability in the SMO structure, with $\theta_A^0 = -\pi/3$ and $k_B = 20k_A = 1\,(\mathrm{N\cdot m})/\mathrm{rad}$. (a) The normalized potential energy with respect to the height H. (b) The force-displacement curve. The two stable configurations are denoted by solid dots H_1 and H_2.

Considering the difficulty in measuring and utilizing the folding angles in applications, it is more convenient to examine the structure in terms of its height. The height H of the SMO structure, defined as the distance between the center vertices of both cells [Fig. 1(a)], can be expressed as

$$H = a_B \sin\theta_B \sin\gamma_B - a_A \sin\theta_A \sin\gamma_A. \tag{5}$$

Hence, the two stable configurations (say, H_1 and H_2) can be determined via

$$\frac{\partial \Pi}{\partial H} = 0, \quad \frac{\partial^2 \Pi}{\partial H^2} > 0. \tag{6}$$

Taking derivative of the potential Π with respect to H, the force-displacement relation can be obtained as

$$F = \frac{\mathrm{d}\Pi}{\mathrm{d}H} = \frac{\mathrm{d}\Pi}{\mathrm{d}\theta_A}\left(\frac{\mathrm{d}H}{\mathrm{d}\theta_A}\right)^{-1}. \tag{7}$$

Hence, on the force-displacement curve [Fig. 3(b)], the two stable configurations are the intersection points with the $F = 0$ axis and with positive slopes.

C. Prototype and static test

Rather than simplifying the origami structure into an equivalent linkage system, we design and fabricate a proof-of-concept origami prototype that retains the feature of rigid facet and hinge-like creases. This prototype is for: (*i*) validating the predicted bistability, (*ii*) measuring

the bistable force-displacement relationship, and (*iii*) implementing dynamic experiments. The origami facets are water jet cut individually from 0.25-mm thick stainless steel sheets. Then they are stuck to a 0.13-mm thick adhesive-back plastic film (Ultra High Molecular Weight (UHMW) Polyethylene) to form two separate Miura-Ori cells (see the Miura-Ori design in Table 1). We paste 0.01-mm thick pre-bent spring-steel stripes at the creases corresponding to the dihedral angles ρ_{B2} and ρ_{B4} to provide strong torsional stiffness (K_{B2} and K_{B4}). The stress-free angle for these pre-bent spring-steel stripes is about 90°, corresponding to a stress-free folding angle $\theta_{A1}^0 \approx 57^\circ$. Then the two Miura-Ori cells are connected along the connecting creases by adhesive films to form a complete SMO structure prototype. Fig. 4(a) schematically illustrates the prototyping steps. The obtained SMO prototype maintains its rigid-foldability because the steel facets are much stiffer than the plastic creases, and the crease stiffness K_{B2} and K_{B4} are significantly higher than the stiffness of other creases (originated from the bending of the films) to generate bistability.

To install the SMO prototype on the universal testing machine and the shaker, we design and 3D-print several connectors [Fig. 4(b)]. The connectors are screwed onto the rectangle steel plates, which are further connected with the SMO prototype at the top and bottom creases through adhesive films. A screw rod can then be inserted into the holes on the connectors and fixed with the connectors so that the relative motions between the top (or bottom) creases are not restricted while the external force can be effectively transmitted to the SMO prototype.

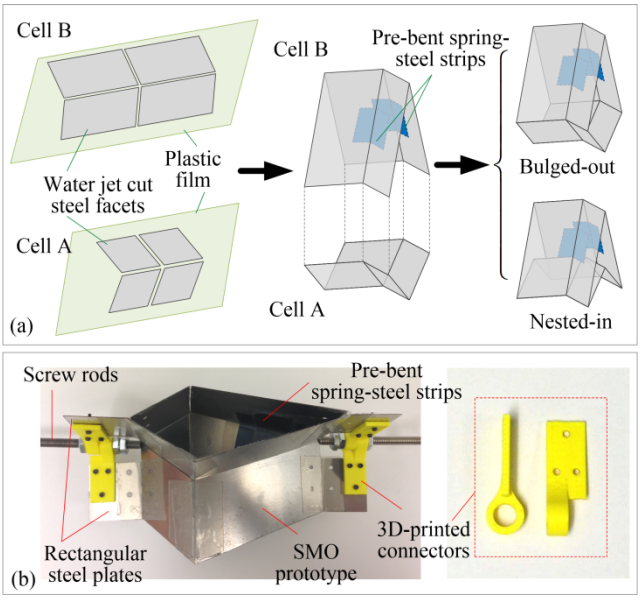

FIG. 4. SMO structure prototype. (a) Illustration of the prototyping method. (b) SMO prototype with 3D-printed connectors and screw rods.

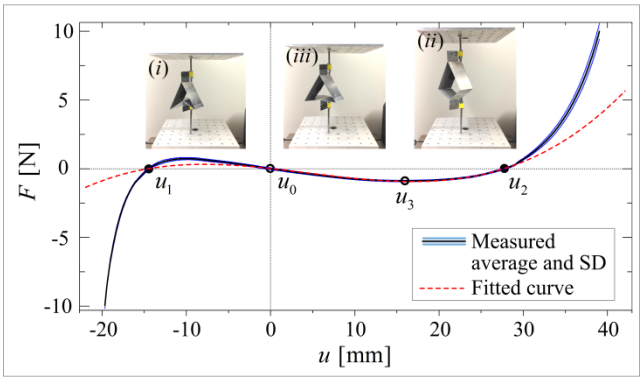

FIG. 5. Measured and fitted force-displacement curves of the SMO prototype. Insects display the prototype at the nested-in configuration (*i*), bulged-out configuration (*ii*), and a middle state (*iii*).

We perform five complete tensile and compression tests on the SMO prototype to derive the force-displacement relationship; for each test, we average the tensile and compression data to get one curve. Averaging over the five tests yields the measured average (solid curve) and the standard deviation (SD, shaded bands) [Fig. 5]. For convenience, we introduce a new coordinate $u = H - H_0$, where $u_0 = 0$ (i.e., $H = H_0$) is set at the unstable equilibrium (in Fig. 5, it is the intersection points with the $F = 0$ axis and with negative slope). The SMO prototype shows strong bistability, with two bistable configurations locating at $u_1 = -14.43$ mm and $u_2 = 27.75$ mm. The insets display the bulged-out and nested-in configurations, as well as an intermediate folding state.

III. DYNAMIC EXPERIMENTS

A. Experimental setup

Fig. 6(a) schematically illustrates the experimental setup for the dynamic test. With the 3D-printed connectors, we are able to connect the SMO prototype onto the shaker and connect a lumped mass with the SMO prototype. The SMO prototype is suspended on a fixed frame with very light strings. We apply harmonic base excitations to the SMO prototype in the horizontal direction (i.e., the height direction of the SMO structure), and use two laser vibrometers to synchronously measure the absolute motions of the shaker and the lumped mass, respectively. The base excitation amplitude maintains a relatively stable value based on preset gain factors. The experimental parameters are listed in Table 2.

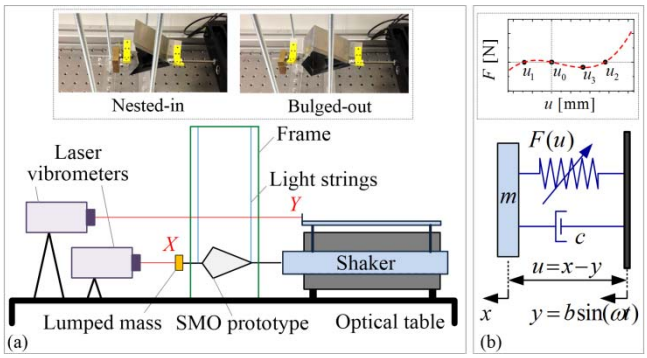

FIG. 6. (a) Schematic illustration of the dynamic experiment setup; insets show the photos of the nested-in and bulged-out configurations of the SMO prototype. (b) Equivalent SDOF model for numerical simulation, inset shows the fitted force-displacement curve.

TABLE 2. Dynamic Experiment Parameters

Parameters	Values
SMO prototype mass	41 g
Lumped mass	89 g
Total mass	135 g
Shake excitation frequency	2 Hz~12 Hz
Shake excitation amplitude (average value and SD)	6.17 mm σ=0.397 mm

B. Displacement transmissibility analysis

The SMO prototype is tested under discrete excitation frequencies from 2 Hz to 12 Hz, with frequency interval of step 0.1 Hz. External perturbations are applied to the lumped mass so as to capture all possible steady-state dynamics. At each excitation frequency ω, the absolute displacement time-histories of the lumped mass (say, X) and the shaker (say, Y) are measured. Considering that the dynamic response of the SMO prototype can be highly nonlinear, we use the root mean square (RMS) value of the displacement data to characterize the average vibrational energy. Dividing the RMS of the lumped mass's steady-state displacement by the RMS of the shaker's excitation displacement, we derive the displacement transmissibility of the SMO prototype in terms of the RMS value:

$$T_{d\_\mathrm{RMS}} = \frac{X_{\mathrm{RMS}}}{Y_{\mathrm{RMS}}} = \frac{\sqrt{\left(x_1^{\,2} + x_2^{\,2} \ldots + x_N^{\,2}\right)/N}}{\sqrt{\left(y_1^{\,2} + y_2^{\,2} \ldots + y_N^{\,2}\right)/N}}, \tag{8}$$

where x_i and y_i ($i = 1, 2, ..., N$) denote the data points in the displacement time-histories; the data time length is selected as the integer multiples (>10) of the excitation period. Fig. 7(a) shows the relationship between T_{d_RMS} and the excitation frequency ω. By examining the $T_{d\_\mathrm{RMS}} \sim \omega$ relationship and the displacement time-histories, two types of responses are identified: intrawell responses that oscillate near one of the stable configurations, and interwell responses that snap between the two stable configurations. The intrawell responses can be around either the nested-in or the bulged-out configuration, which are referred as intrawell (in) and intrawell (out), respectively; the interwell responses can be periodic or chaotic (see descriptions below).

Fig. 7(a) reveals that at certain excitation frequency, multiple types of responses could coexist under different initial conditions. For intrawell vibrations, the intrawell (out) responses have higher transmissibility than the intrawell (in) responses. It is found that at relatively low excitation frequency, the transmissibility is higher than one and increases slowly with ω; while at relatively high excitation frequency, the transmissibility could drop below one, indicating an attenuation of the base excitation. For the interwell vibrations, a much higher transmissibility is detected, suggesting a remarkable amplification of the base excitation. For the periodic case, the transmissibility gradually increases with respect to the excitation frequency; while for the chaotic case, the transmissibility remains fluctuation and is lower than that for the periodic case.

C. Spectrum analysis

Note that the RMS displacement transmissibility analysis offers an overall evaluation of the SMO prototype's performance on transmitting vibration energy. However, this index alone cannot provide detailed dynamic characteristics. To gain in-depth understanding, spectrum analyses are carried out on the response signals. We apply fast Fourier transform (FFT) on X and identify the most significant components, say $\bar{X}_k$ at frequency ω_k. By dividing $\bar{X}_k$ by the base excitation amplitude (say, $\bar{Y}_0$), we derive the displacement transmissibility for each main frequency component:

$$T_{d\_k} = \frac{\bar{X}_k}{\bar{Y}_0}. \tag{9}$$

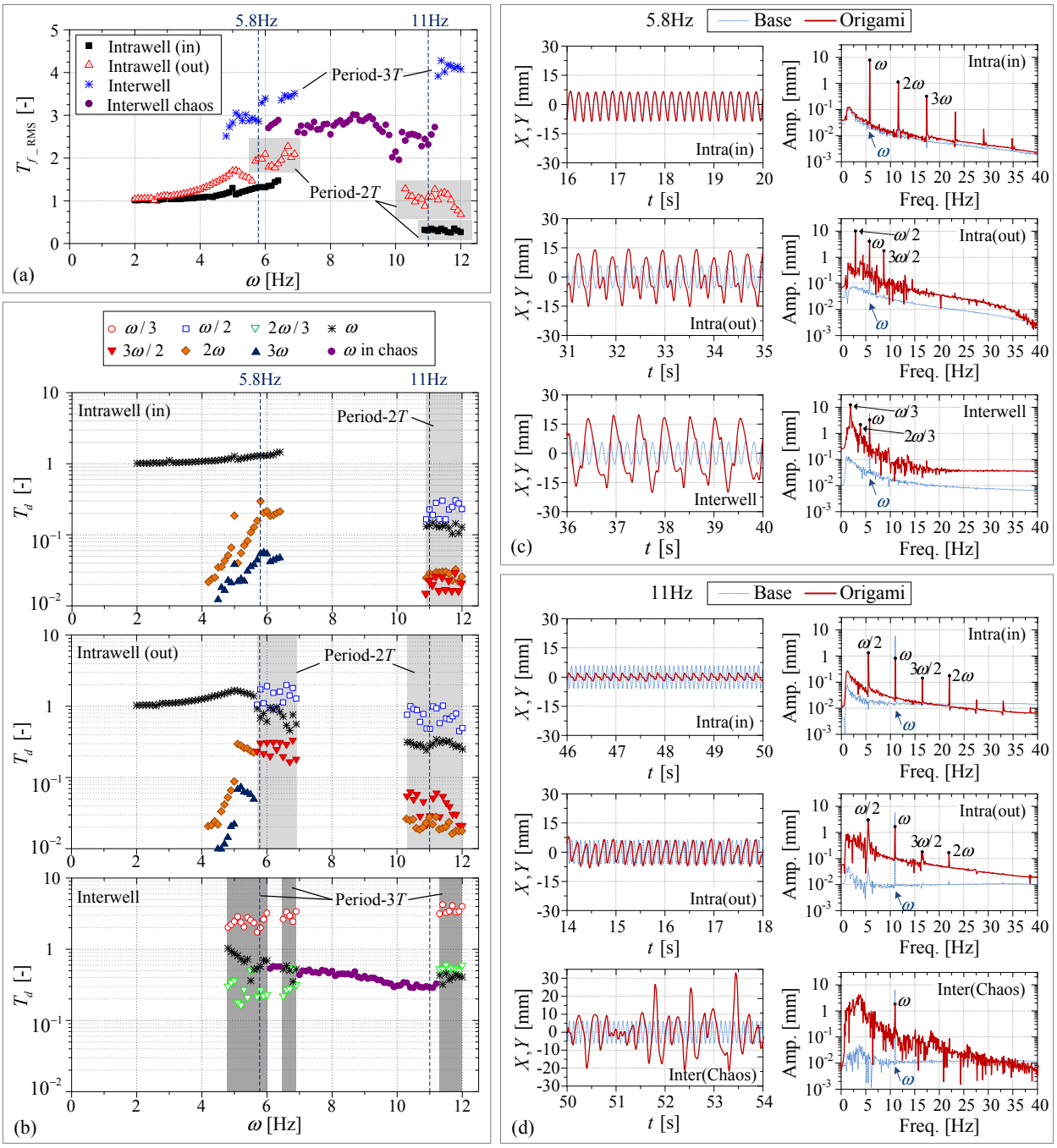

FIG. 7. Experiment results. (a) Displacement transmissibility in terms of the RMS value with respect to the excitation frequency ω. (b) From top to bottom, showing the displacement transmissibility of the main frequency components for the intrawell (in), intrawell (out), and interwell responses, respectively. (c) Three types of responses at $\omega = 5.8$ Hz : from top to bottom, single periodic intrawell (in), $2T$-subharmonic intrawell (out), and $3T$-subharmonic interwell responses. (d) Three types of responses at $\omega = 11$ Hz : from top to bottom, $2T$-subharmonic intrawell (in), $2T$-subharmonic intrawell (out), and interwell chaotic responses. Both the displacement time histories and the FFT spectrums are displayed in (c) and (d), and for reference, the excitation signals are also included.

Fig. 7(b), from top to bottom, shows the displacement transmissibility of the main frequency components for the intrawell (in), intrawell (out), and interwell responses, respectively. For the intrawell responses, it is found that when the excitation frequency is relatively low, the oscillation is a single periodic response dominated by the main harmonic (i.e., ω); 2ω and 3ω super harmonic components with much lower magnitude are also observed in the spectrum. For example, the intrawell (in) response at $\omega = 5.8$ Hz [Fig. 7(c), top] belongs to this type. With the increase of excitation frequency, order-1/2 and order-2 harmonics ($\omega/2$, $3\omega/2$, 2ω) appear. The $\omega/2$ component becomes especially dominant and induces a subharmonic response with period $2T = 2/\omega$; for example, the intrawell (out) response at $\omega = 5.8$ Hz [Fig. 7(c), middle] and the intrawell (in) and intrawell (out) responses at $\omega = 11$ Hz [Fig. 7(d), top and middle].

For the periodic interwell response, spectrum analyses reveal that the order-1/3 harmonics ($\omega/3$, $2\omega/3$) exist. Especially, $\omega/3$ component makes a dominant contribution to the spectrum and induces another subharmonic response with period $3T = 3/\omega$, see the example at $\omega = 5.8$ Hz [Fig. 7(c), bottom]. However, for the irregular interwell response, except the excitation component at frequency ω, no other discrete peaks is identified in the spectrum; instead, continuous frequency band is observed, which is an indicator of chaotic response. Such chaotic response is illustrated via an example at $\omega = 11$ Hz [Fig. 7(d), bottom].

The spectrum analysis provides us with wealth of information for determining the dominant nonlinearities of the SMO structure. For the intrawell vibrations, no matter the single periodic or $2T$-subharmonic, the order-1/2 harmonic components (i.e., $\omega/2$, $2\omega/2$, $3\omega/2$, and $4\omega/2$ components) occupy the majority of the vibration energy, indicating the dominance of the quadratic nonlinearity. While for the periodic interwell vibrations (which is $3T$-subharmonic), the order-1/3 harmonics (i.e., $\omega/3$, $2\omega/3$, and $3\omega/3$ components) plays a major role, suggesting the dominance of the cubic nonlinearity. Overall, spectrum analysis demonstrates that the quadratic and cubic factors dominate the SMO structure's nonlinearities; the observed difference on dominant factors is owing to the disparity of vibration amplitudes in intrawell and interwell responses.

IV. NUMERICAL SIMULATIONS

A. Fitted force-displacement relation and simplified system

The sub-harmonic and super-harmonic components in the dynamic responses indicate that both quadratic and cubic nonlinearity are significant for the origami structural stiffness; we can thus use a third-order polynomial to approximate the measured force-displacement curve. Considering that the equilibrium positions are the most important information to be captured, we use the following polynomial for curve fitting:

$$F(u) = \alpha(u-u_0)(u-u_1)(u-u_2), \tag{10}$$

where u_0=0 denotes the unstable equilibrium, $u_1 = -14.43$ mm and $u_2 = 27.75$ denote the two stable configurations, and α can be determined via an additional point on the curve. Here we choose the point with the maximum negative force (i.e., u_3 in Fig. 5), which gives $\alpha = 0.0001578$, and the fitted force-displacement curve yields

$$F(u) = 0.0001578u(u+14.43)(u-27.75), \tag{11}$$

shown in Fig. 5 with dashed curve.

The fitted curve captures the main characteristics of the measured force-displacement relationship, including the dominant nonlinearities, the stable and unstable equilibriums, and the maximum negative force. However, the fitted curve shows some discrepancy with the measured data when the displacement far exceeds the stable configurations. Taking higher order polynomial is a possible way to address this issue, but may make it more difficult to predict the dynamic responses.

With the fitted force-displacement relation, the undertaken dynamic experiments can be simplified into a single DOF nonlinear system subject to harmonic base excitation, shown in Fig. 6(b). Its equation of motion is

$$m\ddot{u} + F(u) + c\dot{u} = -m\ddot{y}, \tag{12}$$

where m denotes the load mass; $u = x - y$ denotes the relative displacement between m and the base, with $u = 0$ being the unstable equilibrium; $F(u)$ is the fitted force-displacement relation (i.e., Eq. (11)); and c is the viscous damping coefficient. The damping mainly comes from the creases made of plastic films. The base is subjected to a harmonic excitation $y = b\sin(\omega t)$ with amplitude b and frequency ω.

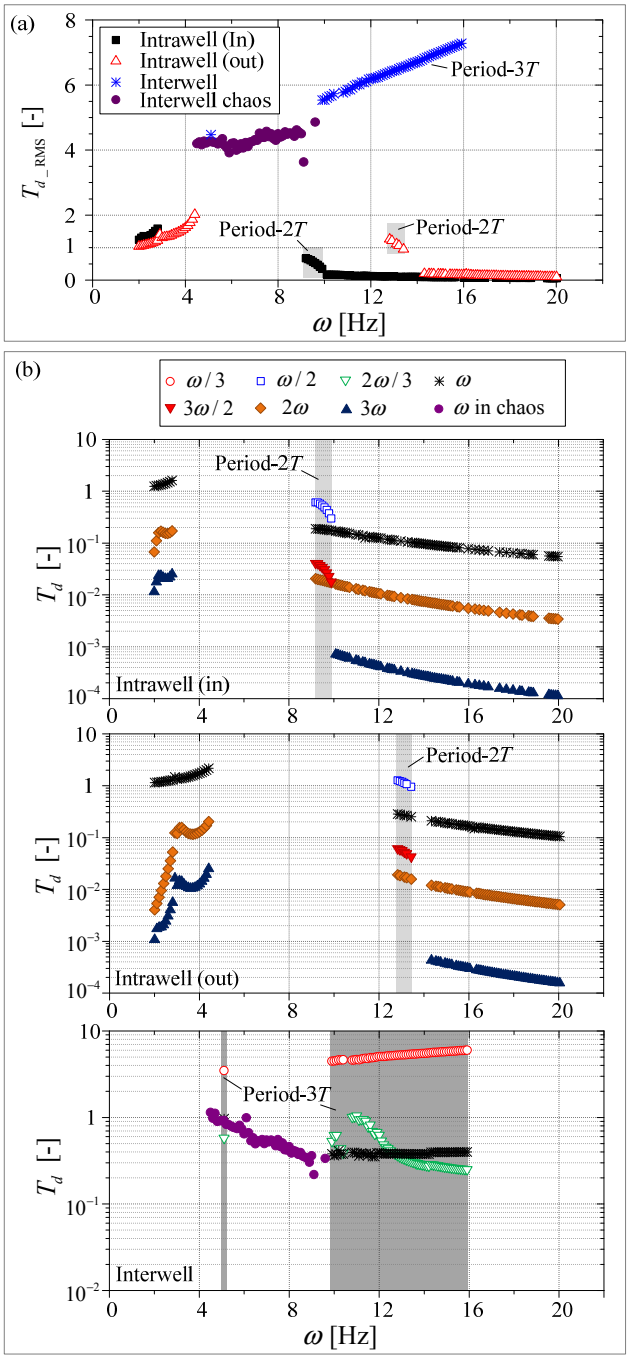

FIG. 8. Numerical simulation results. (a) Displacement transmissibility in terms of the RMS value with respect to the excitation frequency ω. (b) From top to bottom, showing the displacement transmissibility of the main frequency components for the intrawell (in), intrawell (out), and interwell responses, respectively.

B. Numerical simulations

The objective for performing numerical study is to verify whether it is viable to use the quadratic and cubic terms to represent the SMO structure's nonlinearity. If so, the simplified dynamic system (Eq. (12)) should reproduce similar bistable dynamics as those observed in experiments, including the intrawell and interwell responses, the transmissibility, and the spectrum information.

Based on the experimental setup [Table 2], we assign $m = 0.12$ kg, $b = 6$ mm, and $c = 0.6$ kg/s in Eq. (12) for numerical simulations. Eq. (12) is solved in Matlab® through ordinary differential equation solver ODE45. With a step of 0.1 Hz, a discrete frequency sweep is performed between 2 Hz and 20 Hz. At each excitation frequency, three initial conditions $(u_0, \dot{u}_0)$ are used to capture different dynamics: (-14.43, 0), (0, 0), and (27.75, 0). Similar to the experiments, we examine the system's displacement transmissibility in terms of the RMS value (i.e., $T_{d\_\mathrm{RMS}} = y_{\mathrm{RMS}} / x_{\mathrm{RMS}}$) [Fig. 8(a)]. It shows that the system is able to produce intrawell (in), intrawell (out), periodic interwell, and chaotic interwell oscillations. In the intrawell responses, the base excitations could be significantly attenuated at relatively high frequency, while the interwell responses have obvious amplification effects. Applying FFT on these responses, we derive the displacement transmissibility of the main frequency components [Fig. 8(b)]. Simulations indicate that for the periodic intrawell responses, the ω and 2ω components play a leading role; for $2T$ subharmonic intrawell responses, the $\omega/2$, ω, and $3\omega/2$ components dominates; and for $3T$ subharmonic interwell responses, the $\omega/3$, $2\omega/3$, and ω components govern the oscillations.

The numerical simulation results discussed above qualitatively agree with the experiments in terms of the response type, the displacement transmissibility, and the dominant frequency components. It manifests that combined quadratic and cubic nonlinearities could effectively predict the dynamic response of the bistable origami structure. Such a simplified nonlinearity representation provides an efficient and effective approach to analyze such origami dynamics with different designs and bistable characteristics. We remark that the damping coefficient and the excitation amplitude could also significantly affect the origami dynamics; however, investigating their influences is beyond the scope of this study. In addition, a quantitatively accurate verification is possible if the origami facet inertial is considered and more precise stiffness and damping profiles can be obtained.

V. DISCUSSION

The research reported in Sections III and IV have successfully identified the dominant nonlinearities and investigated the dynamic characteristics of the SMO prototype through experimental and numerical studies. These results offered important physical insights and laid down the foundations for more comprehensive analyses of different origami designs and bistable profiles. In this section, we heuristically discuss several analytical tools that could contribute to the in-depth understanding on the dynamics of bistable origami.

A. Stacked Miura-Ori structure and Helmholtz-Duffing Oscillator

Recalling the simplified equation of motion of the SMO structure (i.e., Eq. (12)) and substituting the fitted force-displacement relation (Eq. (10)) and the base excitation into it, we get

$$\ddot{u} - k_1 u + (k_1 - s)u^2 + \frac{\alpha}{m}u^3 + c\dot{u} = p\sin\omega t, \tag{13}$$

where $k_1 = -\alpha u_1 u_2 / m$, $s = \alpha(u_1 + u_2 - u_1 u_2)/m$, $p = b\omega^2$, and $c^* = c/m$ (for clarity, we will leave out the star). Careful observation indicates that Eq. (13) actually represents a Helmholtz-Duffing oscillator (HDO).

In general, an HDO can be expressed as [48]

$$\ddot{z} - \kappa z + (1-\sigma)z^2 + \lambda z^3 + \delta\dot{z} = p\sin\omega t, \tag{14}$$

where κ, σ, δ, and λ are constants. Consider the corresponding conservative system of Eq. (14), the potential function can be expressed as $V(z) = -\kappa z^2/2 + (1-\sigma)z^3/3 + \lambda z^4/4$. When $\kappa < 0$, the potential displays monostability with only one well locating at $z = 0$, see an example with $\kappa = -0.1$, $\lambda = \sigma = 0.3$ [Fig. 9(a)]. When $\kappa > 0$, the potential profile shows bistability: if $\sigma = 1$, $\lambda \neq 0$, the system degenerates into a classical Duffing oscillator with symmetric bistable potential wells; if $\sigma \neq 1$, $\lambda = 0$, the system degenerates into a Helmholtz oscillator with a single-well potential; in more general situations when $\sigma \neq 1$ and $\lambda \neq 0$, the system's twin-well potential shows asymmetry. With $\kappa = 1$ and $\lambda = \sigma$, we plot the bistable potential energy landscapes corresponding to $0 < \sigma \leq 1$ and $\sigma \geq 1$ in Figs. 9(b) and (c), respectively, with $\sigma = 0.4$ and $\sigma = 3$ as examples. The two wells exhibit asymmetry with different depth and different width: when $0 < \sigma \leq 1$, the left well is deeper and wider than the right one; and when $\sigma \geq 1$, the right well is deeper and wider.

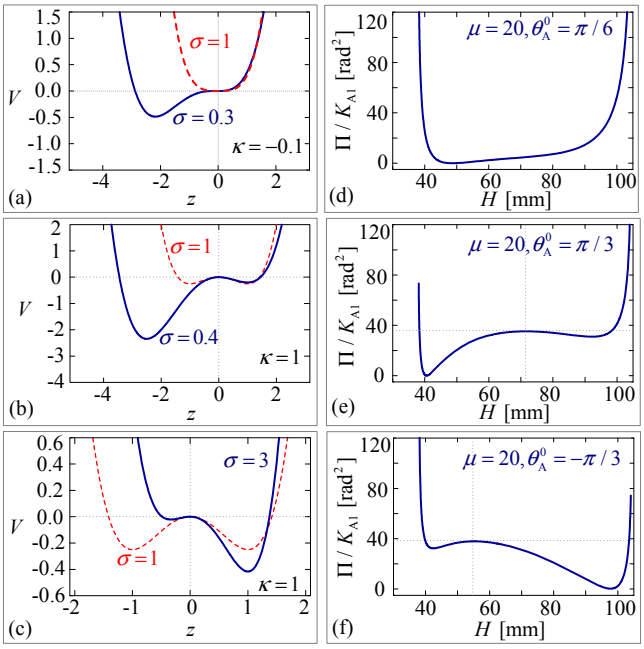

FIG. 9. Similarities between the HDO potential and the SMO potential profiles. (a) ~ (c) show the potential energy landscapes of the HDO at $\kappa = -0.1$, $\sigma = 0.3$, $\kappa = 1$, $\sigma = 0.4$, and $\kappa = 1$, $\sigma = 3$, respectively, denoted by solid curves. For reference, the degenerated situations at $\sigma = 1$ are also plotted with dotted curves. (d) ~ (f) show the potential energy landscapes of the SMO structure with a small stress-free angle $\theta_A^0 = \pi/6$, a nested-in stress-free configuration at $\theta_A^0 = \pi/3$, and a bulged-out stress-free configuration at $\theta_A^0 = -\pi/3$, respectively. The SMO structure's potential is calculated based on Eq. (4) and (5). Comparing the subfigures in the same row could indicate the similarities between the HDO and the SMO potential profiles.

Similarly, the above features and degenerations of the potential profile can also be observed in the SMO structure. Note that the parameters k_1, s, u_1 and u_2 in Eq. (13) cannot randomly take values but depend on the SMO structure design parameters including geometry and torsional stiffness assignment. If the stress-free angle θ_A^0 is close to 0° or the crease torsional stiffness ratio μ is low, the SMO potential would be monostable [Fig. 9(d)], similar to the case shown in Fig. 9(a). Otherwise, if with a larger stress-free angle θ_A^0 or higher torsional stiffness ratio μ, the SMO potential would show bistability. When the SMO structure's stress-free configuration locates at the nested-in stage, we have $-u_1 > u_2$ and $k_1 > s$, indicating that the nested-in well is deeper and wider than the bulged-out well [Fig. 9(e)], similar to the case of $0 < \sigma < 1$ shown in Fig. 9(b). When the stress-free configuration is bulged-out, we have $-u_1 < u_2$ and $k_1 < s$, implying that the bulged-out well is deeper and wider than the nested-in well [Fig. 9(f)], similar to the $\sigma > 1$ case displayed in Fig. 9(d). However, we remark that the SMO structure always possesses a cubic nonlinearity originating from the geometry, and the

asymmetry of the two potential wells is an intrinsic characteristic; therefore, Eq. (13) cannot degenerate into a Helmholtz oscillator without any cubic terms or a classical Duffing oscillator with symmetric bistable potential wells.

Note that the HDO can describe the dynamics of many engineering systems, e.g., one dimensional structural system with an initial curvature [49], ship roll dynamics with wind load and unbalanced cargo load [50], etc. The investigation shown in Fig. 9 indicates that the potential energy profile of the SMO structure resembles those typical of an HDO, and can be effectively tailored by adjusting the stress-free configuration (i.e., θ_A^0 in Fig. 9(c) and (d)). We will systematically discuss in the next subsection on how to program the bistability profile without changing the origami crease pattern.

The HDO has been an active research topic in the field of nonlinear dynamics due to its rich phenomena. A number of analytical tools have been developed and significant insights on HDOs have been developed [48,51–58]. Therefore, considering the SMO structure as an HDO would contribute to the in-depth understanding of the dynamics of bistable origami. For example, the bifurcation and chaos studies on HDOs [48,52] could help us to uncover the mechanisms that generate subharmonic and chaotic responses observed in the experiments and simulations; the change in HDO dynamics with respect to its potential asymmetry level [56,57] could improve our understanding about the effects of tailoring origami bistability; and many analytical and numerical methods for HDO analyses (such as the energy balance method [55,59], harmonic balance method (HBM) [53,54], frequency–amplitude formulation [55], and high-order averaging method [58]) could be employed for accurate response prediction for bistable origami.

B. Programmable bistability

In this subsection, we discuss the potentials to program the bistability profile without changing the origami crease pattern. Providing that the origami crease pattern is fixed, Eq. (4) indicates that the SMO structure's potential energy depends on two factors: the torsional stiffness at the creases and the stress-free angles. These two factors are relatively easier to be tailored than the origami crease pattern. Here we discuss the effects of programming the crease stiffness ratio (μ) and the stress-free angle (θ_A^0) on the structure's bistability.

With the design parameters shown in Table 1, the SMO structure's potential energy is evaluated. Based on whether the structure is monostable or bistable, the $\mu-\theta_A^0$ plane can as divided into three regions, namely, monostable region *I* and bistable regions *II* and *III* [Fig.

10(a)], where the representative potential curves are sketched. In the monostable region *I*, the SMO potential profile is similar as the HDO with $\kappa < 0$ (e.g., Fig. 9(a)); in the bistable region *II*, the SMO potential profile is similar as the HDO with $\kappa > 0,\ \sigma < 1$ (e.g., Fig. 9(b)); in the bistable region *III*, the SMO potential profile is similar as the HDO with $\kappa > 0,\ \sigma > 1$ (e.g., Fig. 9(c)). Therefore, this partition map enables us to simplify the SMO structure into the corresponding HDO system.

In addition to obtaining the boundary between monstability and bistability, the bistable potential profiles are further investigated in terms of the distance between the two stable wells (d), their depths (V_{in} and V_{out}), and the asymmetry level between the two wells [Fig. 10(a)]. Here the potential difference between the two stable wells ($\Delta V = V_{\text{out}} - V_{\text{in}}$) is employed as the index to characterize the asymmetry (denoted by contours in the bistable regions), with a positive value indicating that the bulged-out configuration is more stable (deeper) than the nested-in configuration, and vice versa.

Fig. 10(a) reveals that the bistable potential profile can be effectively programmed by tailoring the θ_A^0 and μ values. If the stress-free angle θ_A^0 is fixed, increasing the stiffness ratio μ can change the SMO structure from being monostable to bistable (e.g., from point a_1 to a_2 [Fig. 10(a, b)]). Inside the bistable regions, increasing μ will significantly deepen the potential wells (e.g., from point a_2 to a_3 [Fig. 10(b)]). However, changing μ does not affect the distance and asymmetry level between the two stable wells significantly. On the other hand, if μ is fixed, θ_A^0 has stronger effects on the bistability profile. Adjusting the stress-free folding angle from nested-in ($\theta_A^0 > 0$) to bulged-out ($\theta_A^0 < 0$) values can fundamentally shift the bistability asymmetry (e.g., from point a_4 to a_7 [Fig. 10(c)]). Moreover, increasing the magnitude of θ_A^0 (e.g., from point a_6 to a_7 [Fig. 10(c)]) can separate the two stable wells further apart and deepen the potential wells, thus significantly strengthen the asymmetry level. Therefore, we show that the SMO structure's bistability can be effectively programmed by tailoring the stress-free configuration and the torsional stiffness ratio. Such qualitative changes of bistability profile will be reflected in the corresponding dynamic equation (i.e., the HDO parameters), which will then significantly change the dynamic characteristics of the bistable origami.

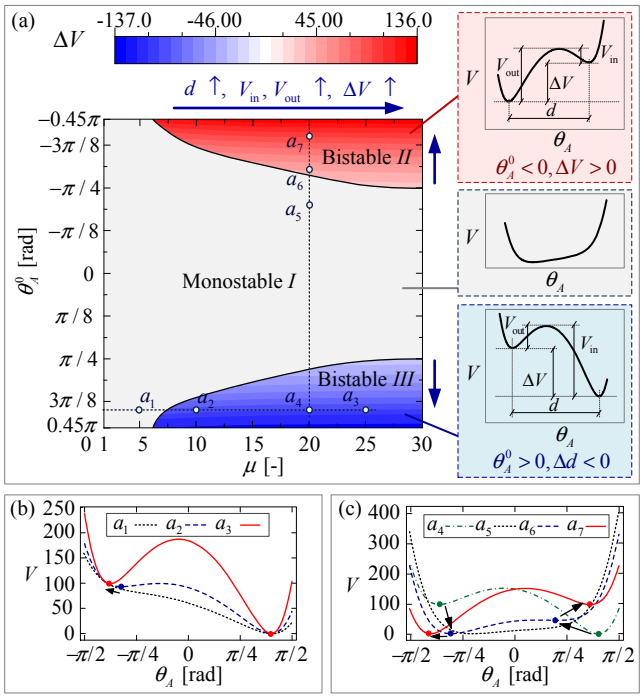

FIG. 10. Programmable bistability. (a) Monostable region *I* and bistable regions *II* and *III* on the $\mu - \theta_A^0$ plane; in the bistable regions *II* and *III*, the contours indicate the potential difference between the two wells (ΔV). Insets show sketches of the monostable and bistable potential curves. The arrows indicate the increase direction of the distance (d), potential depth (V_{in} and V_{out}), and asymmetry level (ΔV). (b) Potential energy landscapes corresponding to points a_1, a_2, and a_3 to illustrate the effects of the stiffness ratio μ. (c) Potential energy landscapes corresponding to points a_4, a_5, a_6, and a_7 to illustrate the effects of the stress-free folding angle θ_A^0. The change of potential well positions are denoted be arrows.

VI. CONCLUSIONS AND PROSPECTIVES

Aiming at advancing the state of the art of origami studies from the static (or quasi-static) to dynamic regime, the presented work investigated the dynamic characteristics of a bistable, stacked Miura-Ori (SMO) structure. Instead of simplifying the origami into a truss-frame system, we designed and fabricated a bistable origami prototype consisting of rigid facets and flexible crease lines with assigned torsional stiffness. We carried out a systematic experimental investigation on the SMO prototype under harmonic base excitations and observed rich dynamic phenomenon that have not been reported. The SMO structure exhibits two types of responses: small-amplitude intrawell oscillation and large-amplitude interwell oscillation, which are able to attenuate or amplify the excitation at different frequencies. Due to the intrinsic geometric nonlinearity, these responses include single-periodic, subharmonic, and even chaotic components.

Spectrum analyses indicate that both quadratic and cubic factors dominate the structural nonlinearities. Due to the difference in response amplitudes, the quadratic nonlinearity plays a leading role in intrawell oscillations, while the cubic nonlinearity dominates the periodic interwell oscillations. Such observations indicate the feasibility of using third-order polynomials to approximate the experimentally measured force-displacement curve of the SMO structure. To verify this extrapolation, we performed numerical simulations with the fitted force-displacement relation. Simulation results manifest the correctness of the identified nonlinearities by capturing the dynamic phenomena observed in experiments.

Through heuristic discussions, we established the parallelism between the SMO structure and the Helmholtz-Duffing Oscillator (HDO) by comparing their potential energy profiles. We noted that the SMO structure's potential profile resembles an HDO, suggesting that the established tools and insights of HDO can be applied in analyzing the bistable origami dynamics. Moreover, we showed that without changing the origami crease pattern, the bistable profile of the SMO structure can be programmed by tailoring the crease stiffness ratio and the stress-free configuration. Such changes in bistability are equivalent to altering the HDO parameters, which will directly affect the system dynamic response.

The bistability in origami structure is highly programmable, not only in terms of the transition between monostability and bistability, but also in terms of the equilibrium positions, the potential well depth, and the asymmetry between the two stable configurations. Such strong programmability would offer the bistable origami structure with great potentials in various dynamic applications. For example, if the origami structure is adopted as an energy harvester, relatively shallow potential wells would be helpful for the triggering of large-amplitude interwell responses with low-excitation levels [36,60]; if the SMO structure is developed as a dynamic motion amplifier, increasing the distance between the two stable configurations will increase the amplification ratio [61].

We also want to remark that with the rigid-foldable assumption, the 3D periodic SMO metamaterial shown in Fig. 1(c) could retain all the kinematical, mechanical and dynamical characteristics of a single SMO unit. In addition, since the origami kinematics is scale-independent, proportionally increasing or decreasing the size would not fundamentally affect the mechanical and dynamical characteristics of the origami structure.

This research performs a comprehensive experimental and analytical investigation on the dynamics of a bistable Miura-ori structure. The findings can significantly advance the state of the

art and open new perspectives for the origami research. It provides a solid foundation for programming origami bistability, tailoring the origami bistable dynamics, and adopting origami metastructures and metamaterials in dynamic applications.

ACKNOWLEDGEMENT

The authors would like to thank Xiaoxu Zhang for the extensive discussions on experimental data processing that were of great benefit to this work. This research was partially supported by the National Science Foundation under Awards 1634545 and 1633952 and the University of Michigan Collegiate Professorship.

REFERENCE

[1] M. J. Harrington, K. Razghandi, F. Ditsch, L. Guiducci, M. Rueggeberg, J. W. C. Dunlop, P. Fratzl, C. Neinhuis, and I. Burgert, Nat. Commun. **2**, 337 (2011).
[2] D. S. A. De Focatiis and S. D. Guest, Philos. Trans. R. Soc. A **360**, 227 (2002).
[3] H. Kobayashi, M. Daimaruya, and H. Fujita, in *IUTAM Symp. Dyn. Adv. Mater. Smart Struct.*, edited by K. Watanabe and F. Ziegler (Springer Netherlands, 2003), pp. 207–216.
[4] T. Tachi, in *Origami4*, edited by R. J. Lang (CRC Press, 2009), pp. 175–187.
[5] T. Tachi, J. Int. Assoc. Shell Spat. Struct. **50**, 2287 (2009).
[6] N. Watanabe and K. Kawaguchi, in *Origami4*, edited by R. J. Lang (CRC Press, 2009), pp. 165–174.
[7] T. Tachi, IEEE Trans. Vis. Comput. Graph. **16**, 298 (2010).
[8] E. D. Demaine and J. O'Rourke, *Geometric Folding Algorithms：Linkages, Origami, Polyhedra* (Cambridge University Press, Cambridge, 2007).
[9] S. Waitukaitis and M. van Hecke, Phys. Rev. E **93**, 23003 (2015).
[10] T. Tachi, in *Adv. Archit. Geom. 2010* (Springer Verlag, Vienna, 2010), pp. 87–102.
[11] J. M. Gattas and Z. You, Eng. Struct. **94**, 149 (2015).
[12] K. Miura, Inst. Sp. Astronaut. Sci. Rep. **618**, 1 (1985).
[13] M. Schenk, A. D. Viquerat, K. a. Seffen, and S. D. Guest, J. Spacecr. Rockets **51**, 762 (2014).
[14] K. Kuribayashi, K. Tsuchiya, Z. You, D. Tomus, M. Umemoto, T. Ito, and M. Sasaki, Mater. Sci. Eng. A **419**, 131 (2006).
[15] S. Felton, M. Tolley, E. Demaine, D. Rus, and R. Wood, Science (80-.). **345**, 644 (2014).
[16] A. a. Evans, J. L. Silverberg, and C. D. Santangelo, Phys. Rev. E **92**, 13205 (2015).
[17] V. Brunck, F. Lechenault, A. Reid, and M. Adda-Bedia, Phys. Rev. E **93**, 33005 (2016).
[18] M. A. Dias, L. H. Dudte, L. Mahadevan, and C. D. Santangelo, Phys. Rev. Lett. **109**, 1 (2012).
[19] Z. Y. Wei, Z. V. Guo, L. Dudte, H. Y. Liang, and L. Mahadevan, Phys. Rev. Lett. **110**, 215501 (2013).
[20] F. Lechenault, B. Thiria, and M. Adda-Bedia, Phys. Rev. Lett. **112**, 244301 (2014).
[21] B. G. Chen, B. Liu, A. A. Evans, J. Paulose, I. Cohen, V. Vitelli, and C. D. Santangelo, Phys. Rev. Lett. **116**, 135501 (2016).
[22] M. Schenk and S. D. Guest, Proc. Natl. Acad. Sci. **110**, 3276 (2013).
[23] H. Yasuda and J. Yang, Phys. Rev. Lett. **114**, 185502 (2015).
[24] H. Fang, S. Li, H. Ji, and K. W. Wang, Phys. Rev. E **94**, 43002 (2016).
[25] J. L. Silverberg, A. A. Evans, L. McLeod, R. C. Hayward, T. Hull, C. D. Santangelo, and I. Cohen, Science (80-.). **345**, 647 (2014).

[26] E. T. Filipov, T. Tachi, and G. H. Paulino, Proc. Natl. Acad. Sci. 201509465 (2015).
[27] S. Li and K. W. Wang, J. R. Soc. Interface **12**, 20150639 (2015).
[28] S. Waitukaitis, R. Menaut, B. G. Chen, and M. van Hecke, Phys. Rev. Lett. **114**, 55503 (2015).
[29] J. L. Silverberg, J. Na, A. A. Evans, B. Liu, T. C. Hull, C. D. Santangelo, R. J. Lang, R. C. Hayward, and I. Cohen, Nat. Mater. **14**, 389 (2015).
[30] H. Fang, S. Li, and K. W. Wang, Proc. R. Soc. A Math. Phys. Eng. Sci. **472**, 20160682 (2016).
[31] S. Li, H. Fang, and K. W. Wang, Phys. Rev. Lett. **117**, 114301 (2016).
[32] H. Yasuda, C. Chong, E. G. Charalampidis, P. G. Kevrekidis, and J. Yang, Phys. Rev. E - Stat. Nonlinear, Soft Matter Phys. **93**, 1 (2015).
[33] H. Yasuda, M. Lee, and J. Yang, in *Proc. ASME 2016 Int. Des. Eng. Tech. Conf. Comput. Inf. Eng. Conf.* (2016), p. DETC2016-59592.
[34] S. Ishida, K. Suzuki, and H. Shimosaka, in *Proc. ASME 2016 Int. Des. Eng. Tech. Conf. Comput. Inf. Eng. Conf.* (2016), p. DETC2016-59699.
[35] R. L. Harne and K. W. Wang, *Harnessing Bistable Structural Dynamics – for Vibration Control, Energy Harvesting, and Sensing* (John Wiley and Sons, 2017).
[36] R. L. Harne and K. W. Wang, Smart Mater. Struct. **22**, 23001 (2013).
[37] M. F. Daqaq, R. Masana, A. Erturk, and D. Dane Quinn, Appl. Mech. Rev. **66**, 40801 (2014).
[38] Z. Wu, R. L. Harne, and K. W. Wang, Trans. ASME-Journal Appl. Mech. **81**, 61005 (2014).
[39] K. A. Singh, R. Kumar, and R. J. Weber, IEEE Trans. Power Electron. **30**, 6763 (2015).
[40] Y. Gerson, S. Krylov, B. Ilic, and D. Schreiber, Finite Elem. Anal. Des. **49**, 58 (2012).
[41] R. L. Harne and K. W. Wang, J. R. Soc. Interface **12**, 20141367 (2015).
[42] D. R. Johnson, M. Thota, F. Semperlotti, and K. W. Wang, Smart Mater. Struct. **22**, 115027 (2013).
[43] R. L. Harne and K. W. Wang, J. Sound Vib. **333**, 2241 (2014).
[44] R. L. Harne and K. W. Wang, Appl. Phys. Lett. **102**, 1 (2013).
[45] D. R. Johnson, R. L. Harne, and K. W. Wang, J. Vib. Acoust. **136**, 31006 (2014).
[46] K. Yang, R. L. Harne, K. W. Wang, and H. Huang, Smart Mater. Struct. **23**, 45033 (2014).
[47] C. Lv, D. Krishnaraju, G. Konjevod, H. Yu, and H. Jiang, Sci. Rep. **4**, 5979 (2014).
[48] H. Cao, J. M. Seoane, and M. A. F. Sanjuán, Chaos, Solitons and Fractals **34**, 197 (2007).
[49] X. Huang, Y. Chen, H. Hua, X. Liu, and Z. Zhang, J. Sound Vib. **345**, 178 (2015).
[50] M. Bikdash, B. Balachandran, and A. Navfeh, Nonlinear Dyn. **6**, 101 (1994).
[51] S. Lenci and G. Rega, Chaos, Solitons and Fractals **21**, 1031 (2004).
[52] G. Rega, in *Bifurc. Chaos; Theory Appl.*, edited by J. Awrejcewicz (Springer-Verlag, Berlin, Heidelberg, 1995), pp. 191–215.
[53] Z. Guo and A. Y. T. Leung, Appl. Math. Comput. **215**, 3163 (2010).
[54] Z. Li, J. Tang, and P. Cai, J. Sound Vib. **332**, 5508 (2013).
[55] D. Younesian, H. Askari, Z. Saadatnia, and M. KalamiYazdi, Comput. Math. with Appl. **59**, 3222 (2010).
[56] H. Simo and P. Woafo, Opt. - Int. J. Light Electron Opt. **127**, 8760 (2016).
[57] S. Jeyakumari, V. Chinnathambi, S. Rajaskar, and M. A. F. Sanjuan, Int. J. Bifurc. Chaos **21**, 275 (2011).
[58] K. Yagasaki, J. Sound Vib. **190**, 587 (1996).
[59] J.-H. He, Mech. Res. Commun. **29**, 107 (2002).
[60] L. Tang, Y. Yang, and C.-K. Soh, J. Intell. Mater. Syst. Struct. **23**, 1433 (2012).
[61] J. Jiang and E. Mockensturm, Nonlinear Dyn. **45**, 1 (2005).